Engineering 59 (2026) 143–157

Contents lists available at ScienceDirect

Engineering

journal homepage: www.elsevier.com/locate/eng

Research
Low Carbon Transformation for Conventional Energies—Review

Experimental Insights into Thermodiffusive Instabilities in Lean Hydrogen Combustion

Tao Li *, Benjamin Böhm, Andreas Dreizler

Technical University of Darmstadt, Department of Mechanical Engineering, Reactive Flows and Diagnostics, Darmstadt 64287, Germany

ARTICLE INFO

Article history:
Received 28 April 2025
Revised 5 August 2025
Accepted 26 September 2025
Available online 30 September 2025

Keywords:
Thermodiffusive instabilities
Lean hydrogen combustion
Turbulence–chemistry interaction
Raman/Rayleigh spectroscopy
Flame imaging

ABSTRACT

As a carbon-free carrier for renewable energies, hydrogen has the potential to contribute to the success of the energy transition. In addition to electrochemical applications, thermochemical applications will continue to play an important role in high-performance energy conversion such as advanced low-emission combustion systems. However, the combustion of hydrogen poses challenges due to its special thermophysical and reaction kinetic properties. Lean combustion is required to minimize primary nitrogen oxide (NO_x) formation. This can lead to thermodiffusive instabilities that affect the internal structures of the reaction zone, the fuel consumption rate, the local equivalence ratios, and the local gas temperatures, thereby affecting primary NO_x formation. The thermodiffusive instabilities have long been known and have been extensively described, primarily through theoretical studies and numerical simulations for simple combustion systems. However, their interaction with turbulence in practical combustion environments remains relatively unexplored, particularly in the context of complex, real-world technical applications. There are few experimental data quantifying the influence of thermodiffusive instabilities on the internal flame structure with respect to the turbulence level. Therefore, the aim of this review is to summarize recent experiments to quantitatively describe the interaction between thermodiffusive instabilities and turbulence. Combustion systems of increasing complexity are considered using laser-optical measurement techniques for elucidating local flame properties. While Raman/Rayleigh spectroscopy is used to quantitatively resolve internal flame structures for unconfined combustion systems, this is not easily possible for enclosed systems under pressure. Instead, the extent to which the reaction zone is affected by thermodiffusive instabilities in interaction with the turbulent flow field is quantitatively assessed using information from laser-induced fluorescence measurements. Consistent with all configurations presented here, the ratio of diffusive to convective time scales plays a critical role in the significance of thermodiffusive instabilities.

1. Introduction

In the course of energy system transformation, chemical energy storage has become increasingly important to compensate for the intermittency and geographical dispersion of renewable energy. Hydrogen (H_2) is widely regarded as one of the most promising—perhaps the most important—chemical energy carrier for storing energy generated from renewable sources. Green hydrogen, produced via electrolyzers powered by renewable electricity, can be utilized in a wide range of applications, including stationary gas turbines, aero engines, internal combustion (IC) engines, and industrial burners. Since most combustion technologies are designed and optimized for fossil fuels, they require substantial adaptation for operation with hydrogen. Lean hydrogen combustion, in particular, offers significant advantages, such as reduced emissions (carbon-free combustion with low NO_x), high thermal efficiency (due to low heat transfer as of low flame temperatures), and improved flame stability (owing to hydrogen's high reactivity). Nevertheless, key challenges remain, including thermodiffusive instability (TDI), hydrodynamic instability, and flashback hazards—all due to hydrogen's high diffusivity and reactivity. Experimental investigations bridging the scales from generic to close to reality combustion systems and employing multi-parameter laser diagnostics provide unique *in situ* insights into flame structure and dynamics, which are crucial for overcoming these challenges.

* Corresponding author.
E-mail address: tao.li@rsm.tu-darmstadt.de (T. Li).

https://doi.org/10.1016/j.eng.2025.09.016

A key aspect of lean premixed hydrogen combustion is the TDI. TDI arises when the Lewis number (*Le*) is less than unity, leading to unbalanced molecular and thermal diffusion. This instability distorts the reaction zone, creating flame curvature: positively curved regions (troughs) experience mass and heat focusing, resulting in higher equivalence ratio (ϕ), temperature (T), and local burning speed (S_B), while negatively curved regions (cusps) exhibit mass and heat defocusing, reducing ϕ, T, and S_B, further intensifying curvature. These dynamics destabilize flame fronts and enhance flame surface area, causing irregular propagation compared to fuels with unity *Le*, superadiabatic flame temperatures (elevating NO_x emissions), and hard-to-predict flame speeds, which strongly depend on *Le* and strain rate.

Practical combustors operate with turbulent flows to increase fuel consumption rates by increasing the flame surface area, according to Damköhler's first hypothesis. Turbulence spans a wide range of kinetic energy scales, each of which interacts differently with molecular diffusion. Even at high turbulence levels, direct numerical simulation (DNS) studies [1,2] indicate that TDI effects influence local flame structures but interact strongly with the underlying turbulence field. This complexity makes TDI challenging to model and predict, yet essential for optimizing combustion systems.

Previous experimental efforts using laser diagnostics to understand the flame–turbulence interactions were reviewed in Refs. [3–7]. Selected examples with high levels of turbulence are briefly discussed in the following. The Lund University piloted jet (LUPJ) burner has been extensively used to study turbulent lean and stoichiometric CH_4/air flames under high Karlovitz (*Ka*) conditions. Zhou et al. [8–10] employed multi-species laser-induced fluorescence (LIF) of CH, CH_2O, HCO, and OH radicals, complemented by Rayleigh scattering and laser Doppler velocimetry (LDV), to analyze flame structure dynamics. Their findings revealed reaction zone broadening and near-homogeneous temperature distributions due to turbulence–flame interactions, though distributed combustion was only observed at the flame tip where turbulence was fully developed. Similar distributed flame front structures were later reported in lean premixed CH_4/air low-swirl flames [9]. Recent extensions of this work include H_2 and NH_3 combustion studies in piloted jet configurations [11,12].

The Sydney premixed piloted jet burner (PPJB) [13–15] has provided critical insights into lean CH_4/air flame structures under turbulence. Using 1D simultaneous Raman/Rayleigh scattering, CO-LIF, and OH-LIF measurements, Dunn et al. [13–15] demonstrated that reaction zone thickness scales with turbulence intensity, highlighting enhanced turbulence–chemistry interactions at higher turbulent kinetic energy. These results align with the LUPJ observations of reaction zone broadening but further quantify the dependence of flame structure on local turbulence properties.

The Michigan high-pilot burner has been instrumental in studying turbulent lean CH_4/air flames in the broken reaction regime, as classified by the Borghi–Peters diagram [16]. Wabel et al. [17,18] and Temme et al. [19] employed simultaneous OH/CH_2O LIF and LDV to characterize spatial flame structures under high turbulence. Their key finding revealed that while the preheat zone thickens significantly compared to laminar flames, the reaction zone remains largely unaffected—a distinctive feature of the broken reaction regime. This behavior was linked to an increased integral length scale within the preheat layer, as later confirmed through combined particle image velocimetry (PIV) and CH_2O-LIF measurements [20]. Building on these results, Skiba et al. [21] proposed a revised regime diagram that narrows the broken reaction zone boundaries, refining predictions for turbulent flame stabilization.

Recent studies have employed advanced multi-scalar diagnostics to elucidate the complex behavior of NH_3/H_2 turbulent premixed jet flames piloted by the McKenna burner. Li et al. [22] and Wang et al. [23] demonstrated multi-scalar measurements using simultaneous NH_3/NH/OH-LIF and Rayleigh scattering, revealing significant discrepancies in turbulent-to-laminar flame speed ratios (S_T/S_L) that underscore differential diffusion effects across preheat and reaction zones. Following this work, Wang et al. [24] demonstrated how both turbulence intensity and hydrogen content alter the spatial alignment of intermediate species isocontours, highlighting *Le*-dependent flame front distortions. Schultheis et al. [25] provided further insights through single-shot 1D Raman/Rayleigh spectroscopy in lean-to-rich $NH_3/H_2/N_2$ flames. The measurements uncovered two key phenomena: ① local oxygen concentration critically governs the NH_3/H_2 molecular ratio across temperature gradients, and ② under rich conditions, NH_3 depletion precedes H_2 consumption, likely due to radical pool effects (H/NH_i) generated during ammonia decomposition. Recently, Li et al. [26] and Chaib et al. [27] demonstrated that the OH-LIF intensity gradient serves as an effective marker for TDI. which were applied to both lean H_2 Bunsen flames [27] and lean $NH_3/H_2/N_2$ flames under extreme turbulence ($Ka \leq 2140$) [26]. These findings collectively advance our understanding of nitrogen chemistry interactions in hydrogen-enriched combustion.

In the context of premixed hydrogen/air flames, lab-scale experiments that resolve internal flame structures to investigate flame–turbulence interactions in atmospheric and pressurized burner flames remain relatively scarce. Chaib et al. [27] reported a correlation between OH-LIF intensity gradients and local flame front curvature in H_2-enriched Bunsen flames. Differential diffusion influences the curvature statistics of the flame surface in laminar and low-turbulence Bunsen flames [28,29]. Global flame consumption speed measurements using techniques such as Mie scattering, OH-LIF, and Schlieren imaging have been comprehensively reviewed by Hochgreb [30], covering both Bunsen-type and spherical flame configurations. The present study focuses specifically on TDI–turbulence interactions in burner stabilized flames; hence, spherical flame experiments are not discussed in detail, although we acknowledge the extensive body of flame imaging literature in this area.

In engine applications, high-speed Schlieren imaging has revealed convection and stretching of H_2 flames due to the underlying turbulent flow field [31]. High-speed chemiluminescence measurements have been used to determine global flame growth rates [32,33]. Leite et al. [33] revealed a strong correlation between overall engine cycle performance and early flame development as evaluated from the evolution of an equivalent flame radius. To resolve local flame wrinkling features OH-LIF was employed by Akleiferis and Rosati [32]. Another work employing SO_2-LIF instead of OH [34] implied that turbulence and volume confinement may counteract TDI effects.

Although theoretical and numerical studies (for example Lipatnikov and Chomiak [3], Aspden et al. [1], Berger et al. [35], Law and Sung [7]) predict the suppression of TDI with increasing turbulence intensity, experimental confirmation remains absents. Resolving this issue requires advanced quantitative diagnostics such as Raman/Rayleigh spectroscopy to probe local thermochemical states. However, conducting controlled hydrogen combustion experiments presents significant challenges, including stringent safety requirements. Furthermore, the turbulence intensities needed to fully mitigate differential diffusion effects, as demonstrated numerically by Aspden et al. [1], are often beyond practical experimental feasibility. This review focuses on resolving this gap by summarizing recent experimental evidence for TDI–turbulence interactions, particularly in lean premixed H_2/air combustion. Our objective is to address three critical aspects:

- How can the effects of TDI on the thermochemical states within the reaction zone be measured quantitatively?

- How do increasing TDI and turbulence properties (canonical shear layer versus anisotropic in-cylinder turbulence) affect TDI?
- How can the interaction between turbulence and TDI be quantified at high pressures where the access for optical diagnostics is very limited?

To address these research questions, we employ a systematic experimental approach that progresses through three combustion configurations: ① laminar flames as a baseline reference; ② atmospheric turbulent jet flames; and ③ expanding turbulent flames at high pressures. This sequence is implemented through three distinct experimental configurations: a laminar Bunsen burner for fundamental studies of polyhedral flames, a turbulent free-jet burner for varying degrees of turbulence over a wide range of *Ka* numbers, and IC engine (ICE) flames for high-pressure conditions of practical relevance. Our investigations particularly focus on how turbulence modifies TDI effects, revealing that TDI dominates in low *Ka* number flames but becomes progressively less significant as *Ka* increases. This transition occurs when the convective transport timescales reduce comparable to or even lower than the characteristic reaction timescales, fundamentally altering the flame dynamics.

This review is presented in the following sections: First, we discuss TDI and the existing evidence for turbulence-mediated suppression in Section 2. Then, we detail the three experimental configurations and their respective operating conditions in Section 3. In Section 4, we describe the advanced multi-scalar laser diagnostics used. Finally, we present and discuss key findings from each configuration in Section 5, culminating in a unified conclusion about TDI–turbulence interactions across different combustion environments in Section 6.

2. Thermodiffusive instabilities

Understanding the behavior of lean hydrogen/air flames in turbulent conditions requires a clear grasp of several fundamental physical concepts. These include preferential diffusion, differential diffusion, TDI, as well as the influence of Lewis and Karlovitz numbers. Some of the terminologies were ambiguously interpreted in the literature and should be first clarified.

Preferential diffusion refers to the unequal rates at which different species within a reacting mixture diffuse [7,36]. In H_2/air flames, H_2—being the lightest molecule—diffuses much faster than O_2 or other mixture components. Closely related to this, differential diffusion more generally refers to the differences in diffusion rates among all chemical species and heat [36]. Unlike in CH_4/air flames, where mass and thermal diffusivities are comparable, the high diffusivity of H_2 introduces strong differential diffusion effects. These can cause spatial separation of mass and heat, leading to non-uniform flame structures. To quantify the differential diffusion, the Lewis number (*Le*) is commonly used. *Le* is defined as the ratio of thermal diffusivity to mass diffusivity of the limiting reactant (typically fuel):

$$Le = \frac{\alpha}{D} \tag{1}$$

where α is the thermal diffusivity and D is the mass diffusivity. In lean hydrogen combustion, *Le* is below unity, indicating that mass diffusion dominates over thermal diffusion. Depending on the magnitude of the *Le* number, this enhances TDI, increases flame surface area, and modifies flame stretch response.

The TDI is an intrinsic phenomenon in lean hydrogen/air flames with $Le \ll 1$, reported in previous reviews by Law and Song [7], Lipatnikov and Chomiak, [3,37], Steinberg et al. [4], and Driscoll et al. [6]. Fig. 1 illustrates a schematic of a TDI flame front (color coded by its local curvature), separating burned and unburned gas mixtures. When a small perturbation is introduced, the flame surface develops wrinkles, forming regions of positive (reddish, trough region) and negative (bluish, cusp region) curvature. In areas of positive curvature, H_2—owing to its high diffusivity—diffuses rapidly from the unburned to the burned side (shown by red arrows). Simultaneously, thermal diffusion, which is slower, carries heat in the opposite direction (black arrows). This differential diffusion of fuel and heat results in a local enrichment of H_2 and an increase in temperature near the curved flame tip. The combined effect leads to localized fuel and heat focusing, creating pockets with higher equivalence ratios and post-flame superadiabatic temperatures relative to the globally lean conditions. These regions burn more intensely and propagate further into the unburned mixture, amplifying the local positive curvature. Conversely, in negatively curved regions, H_2 and heat are defocused. The result is a local reduction in reactivity, slower burning, and further deepening of the negative curvature. This feedback loop reinforces the curvature asymmetry and promotes continuous amplification of flame surface perturbations. Overall, the interplay of differential diffusion and flame front curvature leads to an inherently unstable flame structure, characterized by significant variability in local thermochemical states and surface topology.

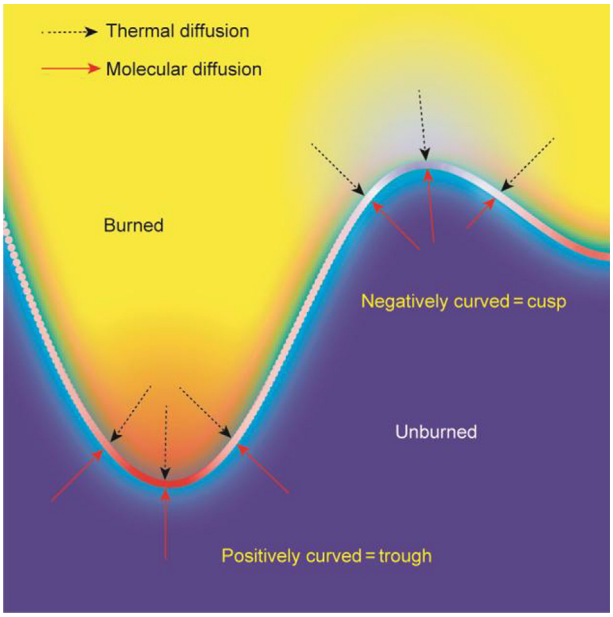

Fig. 1. A schematic showing a flame front color-marked by its local curvature and the molecular and thermal diffusion with *Le* < 1.

For a given lean H_2/air mixture, the significance of TDI depends critically on the relative magnitudes of two competing time scales: the chemical reaction time and the turbulent time scales governing the transport of mass and heat. This interaction between turbulence and chemistry—often referred to as turbulence–chemistry interaction (TCI)—plays a central role in determining flame structure, stability, and propagation characteristics. To systematically classify these interactions, premixed flames subject to turbulent flows are commonly mapped onto different regimes using the Borghi–Peters regime diagram [16], as illustrated in Fig. 2. This diagram organizes flame behavior based on key non-dimensional parameters, primarily the turbulent Reynolds number (Re_T) and the Karlovitz number (*Ka*), which together characterize the scale and intensity of turbulence relative to flame structure. In particular, *Ka* is used to quantify the interaction between the smallest

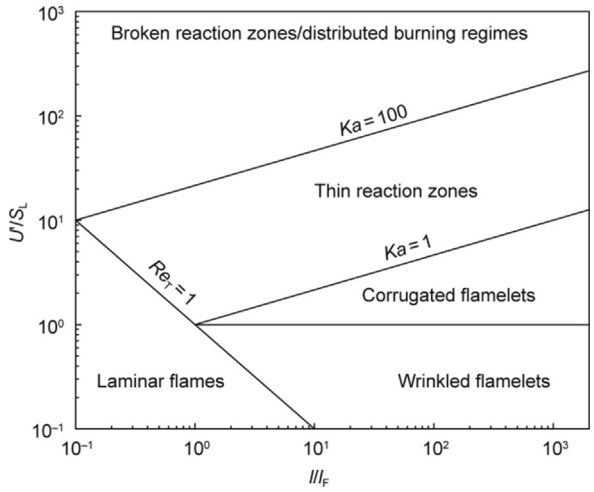

Fig. 2. The Borghi–Peters regime diagram of premixed turbulent combustion.

turbulent eddies and the flame front. It is defined as the ratio of the chemical time scale to the Kolmogorov time scale of turbulence, expressed as [16]:

$$Ka^2 = \left(\frac{\tau_F}{\tau_\eta}\right)^2 = \left(\frac{U'}{S_L}\right)^3 \left(\frac{l_F}{l}\right) \quad (2)$$

where τ_F and τ_η indicate the flame time scale and the Kolmogorov length scale of turbulence, respectively. U' is the root-mean-square (rms) turbulent velocity, l is the integral length scale of turbulence, and l_F is the laminar flame thickness. A high Karlovitz number implies that small-scale turbulence can penetrate and disturb the internal flame structure, potentially altering local burning rates and promoting phenomena such as local extinction, flame stretch, or reignition [16].

The turbulent Reynolds number is defined as:

$$Re_T = \frac{U'}{S_L}\frac{l_F}{l} \quad (3)$$

Following Peters [16], turbulent combustion is represented by $Re_T > 1$ in Fig. 2. For $Ka < 1$, the Kolmogorov scale η is larger than the thermal flame thickness l_F, meaning that the smallest turbulent eddies are unable to penetrate the flame's internal structure. In this regime, the flame front remains thin and coherent, merely wrinkled or corrugated by turbulence, while retaining its laminar substructure, which is commonly referred to as the flamelet regime. As the Karlovitz number increases to the range $1 < Ka < 100$, the Kolmogorov scale becomes smaller than the thermal flame thickness but is still larger than the thickness of the inner reaction zone (approximately $0.1l_F$). Under these conditions, the preheat zone becomes increasingly influenced by turbulence, resulting in a broadened thermal structure, while the main reaction zone remains relatively intact. This regime is often referred to as the thin reaction zones regime. At sufficiently high turbulence intensities, where $Ka > 100$, the smallest eddies become capable of penetrating even the inner reaction zone. This leads to the regime of broken reaction zones (turbulence intensity is high enough to disrupt the coherent flame front structure [16]), and under extreme turbulence, to distributed combustion regime (turbulence becomes so intense that mixing timescales dominate over reaction timescales [2]).

Using numerical simulations, effects of turbulence on TDI in lean H_2/air flames has been previously reported, such as in Refs. [1,2,35,38–42]. Aspden et al. [38] investigated TCI in lean premixed H_2/air flames using DNS, spanning a range of Karlovitz numbers Ka from 1 to 36 within the thin reaction zone regime, and extending up to Ka = 1562 in the distributed burning regime [1]. As Ka increased from 1 to 36, their results revealed increasingly intense local burning, particularly in regions of positive curvature, where both superadiabatic temperatures and elevated fuel consumption rates were observed. This behavior was attributed to the combined effects of enhanced mixing and TDI, which tend to focus fuel and heat in positively curved flame segments. Further supporting this trend, Howarth et al. [42] reported a clear correlation between increased local flame speed and positive curvature over the same Ka range, highlighting the influence of curvature–turbulence coupling in intensifying local reaction rates. A transition to distributed burning was observed when Ka was increased to 1562, where the flame structure no longer retained a distinct reaction zone. This regime was characterized by a nearly linear H_2 consumption profile and a flattened distribution of local equivalence ratio versus temperature, indicating that turbulent transport had overwhelmed molecular diffusion in the scalar mixing processes. In this regime, traditional flamelet assumptions break down, and combustion occurs in a highly mixed, volume-filling manner where chemical reactions are distributed throughout the flow field. However, reaching the distributed combustion regime requires extremely high turbulence or Ka number, which is difficult to achieve experimentally [1].

3. Combustion devices

Three combustion devices were employed to investigate TDI in lean premixed hydrogen/air flames. Fig. 3 highlights the key features of each configuration; additional details can be found in our previous publications. The simplest configuration, a laminar Bunsen jet burner (LBJB), serves as an ideal platform for quantifying TDI in laminar flows, which produces characteristic cellular flame structures in lean hydrogen/air flames [28,45]. For turbulent conditions, a piloted turbulent jet burner (PTJB) enables stabilization of lean premixed hydrogen/air flames at high Karlovitz numbers, extending into the distributed combustion regime [43,44]. To examine realistic conditions under pressure, an optical engine configuration allows observation of premixed flame structures developing under varying engine speeds [34,46]. Two operating conditions were selected for each configuration, with parametric variations designed to emphasize turbulent effects on TDI manifestation. These cases are summarized in Table 1 and described in the following.

(1) LBJB. A laminar Bunsen free-jet burner was used to study polyhedral flames, as shown schematically in Fig. 3(a). The burner consisted of a 16 mm diameter central jet nozzle. The wall thickness was 0.5 mm to minimize heat losses to the tube associated with a recirculating flow at the exit. The jet flow was concentrically surrounded by a coflow of nitrogen with a diameter of 67 mm. As detailed in Table 1, premixed H_2/CH_4/air mixtures with an equivalence ratio of 0.53 and an H_2 content of 79 vol% exited the jet. For this mixture, an effective Lewis number Le_{eff} of 0.58 was obtained according to the volume fraction weighted average formulation following Bouvet et al. [47]. For otherwise constant inflow boundary conditions, residence times were varied with two bulk velocities of 1.65 and 2.50 m·s^{-1} using electronic mass flow controllers. The nomenclature of the flames is defined as HβPγUε, where β represents the H_2 percentage in the fuel, γ denotes the global equivalence ratio of the inflow (ϕ_{global}), and ε represents the bulk velocity (U_0). Two flame cases H079P053U165 and H079P053U250 with different U_0 are discussed in this study.

The properties of an unstretched planar laminar flame such as thermal flame thickness l_F and laminar flame speed S_L were calculated by Cantera 2.5, using the mechanism of Mei et al. [48] and a

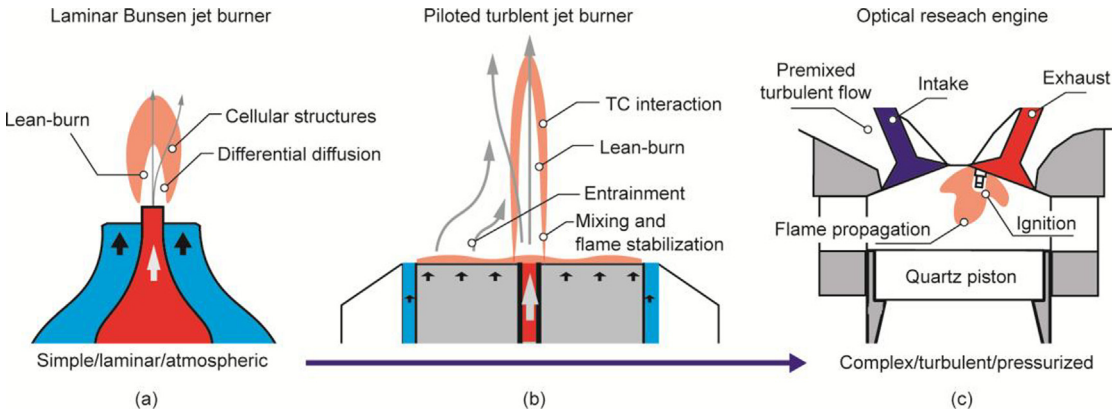

Fig. 3. Schematics of the combustion facilities and underlying processes of interest. (a) Laminar Bunsen jet burner (LBJB), (b) piloted turbulent jet burner (PTJB), and (c) optical ICE.

Table 1
Operating conditions of laminar polyhedral flames, turbulent jet flames, and ICE flames under pressure.

Case	U_0 (m·s^{-1})	Engine speed (rpm)	ϕ_{global}	Le_{eff}	T_{ad} (K)	S_L (m·s^{-1})	l_F (mm)
Laminar polyhedral flames							
H079P053U165	1.65	–	0.53	0.580	1610	0.22	0.63
H079P053U250	2.50	–	0.53	0.580	1610	0.22	0.63
Turbulent jet flames							
H100P040U050	50	–	0.40	0.372	1427	0.24	0.60
H100P040U200	200	–	0.40	0.372	1427	0.24	0.60
ICE flames							
H100P040R400	–	400	0.40	0.390	1427	0.24	0.60
H100P040R800	–	800	0.40	0.400	1427	0.24	0.60

multi-component transport model including the Soret effect. The adiabatic flame temperature T_{ad} was derived from the equilibrium temperature of the H_2/air mixture using a hydrogen–oxygen sub-mechanism from GRI-Mech 3.0.

(2) PTJB. Premixed turbulent flame were investigated in a PTJB, as schematically shown in Fig. 3(b). The burner consists of a central tube with an inner diameter of D_{nozzle} = 4.5 mm providing a fully developed turbulent jet, surrounded by a water-cooled concentric porous sintered stainless steel pilot plate and an outer porous sintered bronze coflow ring. Electronic mass flow controllers were used to vary the gas supply to the jet, pilot, and coflow.

This study focuses on two lean premixed H_2/air turbulent flames, as listed in Table 1. For a fixed global equivalence ratio of 0.4 at the inflow of the jet and pilot flame, the jet bulk velocity U_0 was increased from 50 to 200 m·s^{-1}. Following the nomenclature introduced above, these two cases are named as H100P040U050 and H100P040U200. The pilot flame was operated at a constant inlet velocity (2.5 m·s^{-1}) to produce a slightly lifted flat flame with minimal heat loss to the porous pilot burner. The globally constant equivalence ratio (ϕ_{global}) guaranteed a fully premixed flame in the region of interest. To minimize secondary air entrainment, the coflow was operated with N_2 at a constant flow velocity of 1 m·s^{-1}. Other cases are discussed in Refs. [43,44].

(3) Optically accessible ICE. Flame dynamics and flame structure evolution in the early phase of combustion were investigated in a single-cylinder four-stroke engine equipped with a pent roof cylinder head [46,49,50]. A sketch is shown in Fig. 3(c). The cylinder head was heated to 60 °C. The geometric compression ratio was 8.7. Optical access to the combustion chamber was provided through the piston and a fused silica liner. The engine was operated with port fuel injection [34]. The hydrogen was mixed with the air in the intake manifold 540 mm upstream of the intake valves at a pressure of 0.95 bar. A homogeneous mixture with an equivalence ratio of ϕ_{global} = 0.4 was used. The engine speed was varied from 400 to 800 revolutions per minute (rpm). To obtain the same peak cylinder pressure of 20.5 bar, the ignition timing was set at 25.6° crank angle (CA) before top dead center (TDC) at 400 rpm and 16.6° CA before TDC at 800 rpm. Consequently, the cylinder pressure at the instant of ignition was different. This resulted in slightly different effective Lewis numbers Le_{eff} of 0.39 for 400 rpm and 0.4 for 800 rpm. The measured cylinder pressure curves and the gas properties were derived from Cantera calculations.

4. Laser diagnostics and data evaluation

Several laser diagnostics were used to measure TDI in different hydrogen combustion devices, including 1D Raman/Rayleigh spectroscopy, 2D Rayleigh thermometry, OH-planar LIF (PLIF), and high-speed SO_2-PLIF. Based on the instantaneous *in situ* multi-scalar data, TDI markers are quantitatively determined, allowing for assessment of the turbulence effect on the significance of TDI.

4.1. Quantitative 1D Raman/Rayleigh spectroscopy

Simultaneous 1D Raman/Rayleigh spectroscopy was used to quantify the thermochemical states in the polyhedral and turbulent jet flames by measuring the temperature and mole fractions of the major species (H_2, H_2O, O_2, N_2; for the H_2/CH_4 fueled polyhedral flame in addition CO_2, CO, and H_2O) with high spatial resolution. The local flame structure was determined quasi-simultaneously by 2D Rayleigh scattering. As detailed in Ref. [51], the excitation lasers consisted of four frequency-doubled Q-switched Nd:YAG lasers. The four individual pulses were temporally stretched to about 500 ns by three optical delay lines and focused into the probe volume by a planoconvex lens (f = 600 mm). The focused beam had a waist diameter of 190 μm ($1/e^2$) along the 6 mm probe volume and an energy of about

1.8 J per pulse. The Raman/Rayleigh scattered light was collected by a custom-built spectrometer, as shown in Fig. 4 [44]. The spatial resolution of the achromatic lens was about 60 μm. The Rayleigh scattered signal was spectrally separated from the Raman scattered signal by a dichroic long pass filter and recorded by a thermo-electrically cooled front-illuminated charge-coupled device (CCD) camera. The s-polarized part of the Raman signal, transmitted through a polarization filter and a long-pass filter, was diffracted by a transmission grating before being recorded by a thermoelectrically cooled back-illuminated CCD camera. A customized rotating mechanical shutter was used to reduce background noise, resulting in gating times of 3.4 and 361 μs for Raman and Rayleigh imaging. On-chip spatial binning was applied to the Raman (by four pixels) and Rayleigh (by two pixels) cameras, resulting in projected spatial resolutions of 50 and 20 μm superpixel, respectively.

In the data analysis, 1D Raman data were denoised using a wavelet denoising algorithm. Then the 1D Raman/Rayleigh data were processed by the hybrid matrix inversion method [52]. The temperature dependence of the Raman cross section and cross talk, the normalization of the non-uniform throughput of the 1D Raman signal, and the calibration factors of the Raman responses and cross-talks are taken from Ref. [28]. Exemplified here for the H_2 fueled turbulent jet flame, based on the fuel/oxygen balance of the three major species derived from the 1D Raman/Rayleigh measurements, the local equivalence ratio, ϕ_{local}, shown for both experiments and simulations was calculated as follows [53]:

$$\phi_{local} = \frac{X_{H_2} + X_{H_2O}}{2X_{O_2} + X_{H_2O}} \quad (4)$$

where X_i is the mole fraction of specie i (i = H_2, O_2, or H_2O). For the H_2/CH_4 fueled polyhedral flame a similar procedure was followed, outlined in Refs. [28,43].

Representative values for the precision and accuracy of the measurements are listed in Table 2. The precision of single-shot data is represented by the standard deviation divided by the estimated mean of 100 samples in the product gas of a H_2/air Hencken-type calibration flame at the listed equivalence ratio. The accuracy is based on the repeatability of the calibrations and the deviations of the Hencken-type flame measurements from the corresponding numerical laminar flame simulations.

Table 2
Estimated precision and accuracy in temperature and mole fractions at representative flame conditions.

Scalar	Precision (%)	Accuracy (%)	Equivalence ratio ϕ
T	1.3	2.0	1.0
ϕ	7.4	2.6	1.0
X_{H_2}	9.6	8.4	1.3
X_{H_2O}	3.0	2.0	1.0
X_{N_2}	3.0	1.0	1.0

4.2. Quantitative 2D Rayleigh thermometry

The quantitative 1D Raman/Rayleigh measurements were combined with 2D Rayleigh scattering to visualize the 2D flame structure and to quantify the temperature field around the 1D Raman/Rayleigh probe volume. One microsecond prior to the 1D Raman/Rayleigh measurement, instantaneous flame topologies were visualized by 2D Rayleigh scattering using two laser cavities of a frequency-tripled, Q-switched Nd:YAG laser delivering a total pulse energy of approximately 300 mJ at 355 nm. The laser intersected the 1D Raman/Rayleigh probe volume as a thin sheet with a height of 4.5 mm and a thickness of approximately 400 μm ($1/e^2$). The planar laser beam was tilted by 8°, allowing individual beam paths for 2D Rayleigh and 1D Raman/Rayleigh excitation lasers. The 2D Rayleigh scattered light was collected using a complementary metal–oxide–semiconductor (CMOS) camera coupled to an image intensifier, an ultraviolet (UV) lens (f = 105 mm, f/2.8), and a bandpass filter (355 ± 10 nm). The field of view (FOV) of the 2D Rayleigh camera was (24 × 20) mm^2 with a pixel

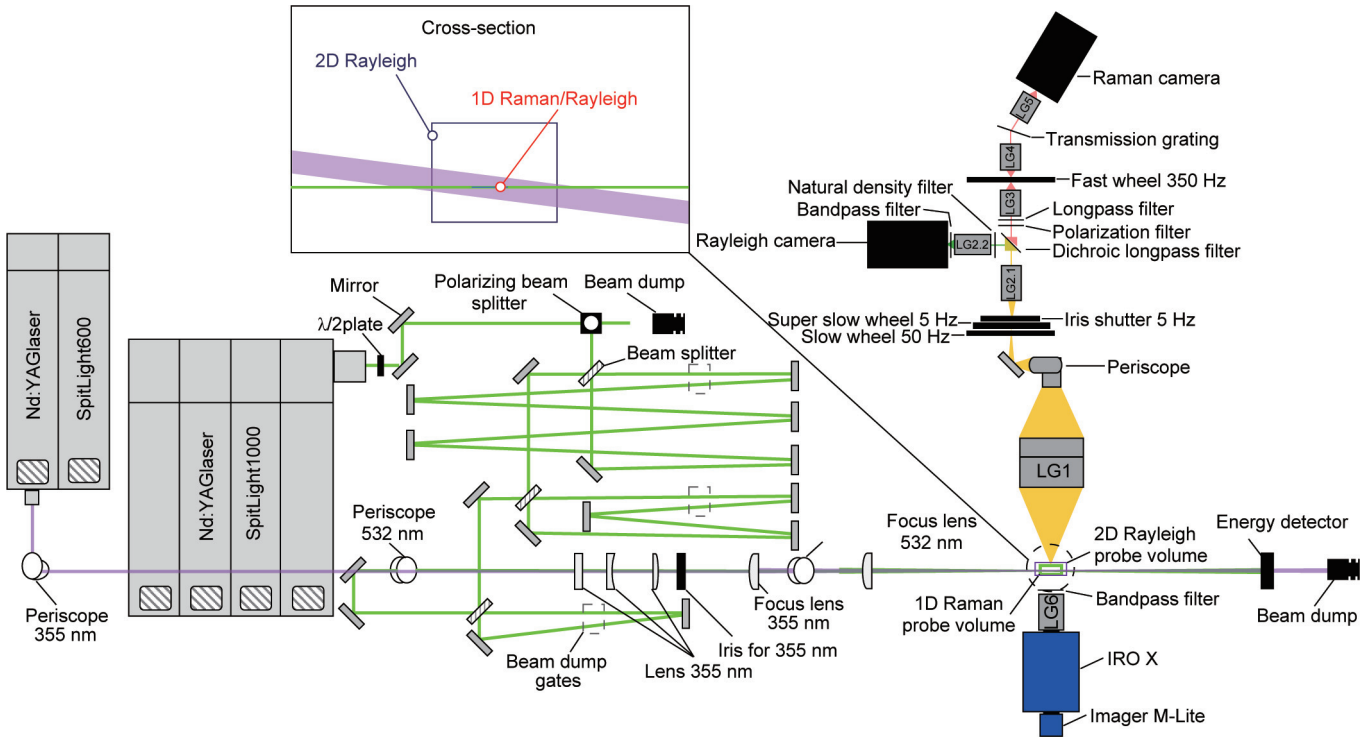

Fig. 4. Schematics of the optical systems for simultaneous 1D Raman/Rayleigh and 2D Rayleigh scattering measurements [44].

resolution of 20 μm. The 1D Raman, 1D Rayleigh, and 2D Rayleigh signals were mapped to each other in the data analysis.

To calculate the temperature (T) from the measured 2D Rayleigh signal intensity (S_{Ray}), the thermochemical states of the premixed H_2/air flames with inlet ϕ ranging from 0.3 to 0.8 were simulated by Cantera with a freely propagating flame model, and used to calculate the corresponding effective Rayleigh scattering cross-section ($\sigma_{Ray,eff} = \sum_1^i X_i\sigma_i$) of the gas mixtures, in which X_i is the mole fraction of the specie i, and σ_i is the Rayleigh scattering cross-section of specie i. The derived $\sigma_{Ray,eff}$ normalized by the unburnt gas mixture ($\sigma_{Ray,reactant}$) over temperature is shown in Fig. 5(a) by the solid lines. The ratio $\sigma_{Ray,eff}/\sigma_{Ray,reactant}$ increases slightly with temperature as ϕ increases from 0.3 to 0.8, as the $\sigma_{Ray,eff}$ is dominated by the majority component of N_2 in the mixture. The simulated $\sigma_{Ray,eff}$ and temperature can be used to deduce the S_{Ray} as follows:

$$\frac{S_{Ray}}{S_{Ray,reactant}} = \frac{T_{reactant}\sigma_{Ray,eff}}{T\sigma_{Ray,reactant}} \quad (5)$$

The corresponding S_{Ray} normalized by the Rayleigh signal intensity in the unburnt gas mixture ($S_{Ray,reactant}$) over temperature are shown in Fig. 5(a) by the dashed lines. The curves overlap with each other, indicating the insensitivity to the local mixture composition, which facilitates the temperature derivation from the Rayleigh scattering signal. In turbulent flames, strain and curvature affect the correlation between the temperature and the normalized S_{Ray}. The $\sigma_{Ray,eff}$ and S_{Ray} was simulated with strain rates ranging from 1000 to 6000 s^{-1} at a constant ϕ of 0.4, as shown in Fig. 5(b). The results indicate that the 2D Ray thermometry is insensitive against strain variation.

4.3. Qualitative LIF imaging

Single-shot imaging of hydroxyl radicals (OH) by PLIF (OH-PLIF) was used to visualize the intrinsic instabilities of H_2/CH_4/air polyhedral flames to quantify the local curvatures of the positively and negatively curved sections of the reaction zones, and to quantify the cell number along the circumferential direction. The OH radical was electronically excited at its A-X (0–1) transition using a 10 Hz Nd:YAG laser-pumped frequency-doubled dye laser operating at approximately 283 nm. The laser beam was formed into a horizontally aligned light sheet (110 μm thick) intersecting the polyhedral flame 5 mm above the burner. Synchronized to the laser pulse, the red-shifted fluorescence was recorded from above using an image intensified CMOS camera equipped with a UV lens (CERCO, f = 100 mm, f/2.8) and a bandpass filter (315 ± 15 nm). The spatial resolution was 125 μm, determined by a sector star and using a cut-off of 14%. Since the polyhedral flames burned stationary, 300 single images were averaged. A similar OH-PLIF setup, but with a vertically aligned laser light sheet intersecting the flame at its central axis, was used to visualize the reaction zone structure and to measure the flame surface curvature in the turbulent H_2 fueled jet flames, while more detailed descriptions are given in the previous work [45].

High-speed imaging of sulfur oxide (SO_2) by PLIF [34,54] was used to visualize the flame front and determine the local flame curvature in the H_2 fueled ICE. For this purpose, 1.1 vol% SO_2 was added to the combustion air in the intake manifold. When excited at 266 nm, the SO_2 fluorescence intensity follows the local gas temperature, as has been studied in detail for CH_4 flames [54]. The advantage over the OH-PLIF method is that a frequency-quadrupled Nd:YAG laser can be used directly instead of a tunable dye laser, which greatly simplifies the experimental setup.

A diode-pumped, frequency-quadrupled Nd:YAG laser (Edgewave) was used as the excitation laser for SO_2 with a pulse repetition rate of 6 kHz (400 rpm) and 8 kHz (800 rpm) to follow the flame evolution with a resolution of 0.4° and 0.6° CA, respectively. The pulse energy was about 600 μJ and the laser light sheet had a width of 5 mm and a beam waist of 160 μm in the region of interest. The laser light sheet was introduced into the cylinder from below through the piston window, which is shown in Fig. 3(c).

Red-shifted fluorescence was recorded through a long-pass filter (276 nm) using a high-speed UV camera (without image intensifier for higher spatial resolutions) and a UV lens (CERCO, f = 100 mm, f/2.8). Astigmatism caused by the curved liner glass was reduced using a +2000 mm cylindrical lens, improving the optical resolution [55]. Spacer rings were used between the camera and the lens, resulting in a magnification of 1.17 for a region of interest of (5 × 15) mm^2. Using a sector star, an optical resolution of about 75 μm (full width at half maximum of the point spread function) was achieved. According to Refs. [40,41], this is sufficient for pressures of 20 bar and 700 K to observe cellular structures as a result of TDI for ICE conditions.

The SO_2-PLIF images were smoothed using a wavelet-based denoiser that preserves edges and gradients in the image while taking into account the camera characteristics. The pixels were then transformed into physical space dimensions using high-resolution target images with a third-order polynomial. Regions with high scattered radiation intensities were masked (spark plug, piston) and the individual images were normalized to the mean laser beam profile. After normalization to the maximum value, the images were binarized using a thresholding method [56]. Closed structures and flame fronts shorter than 30 pixels were removed. Based on the first guess of the flame front identified by the thresholding algorithm, a ±15 pixel wide mask was defined

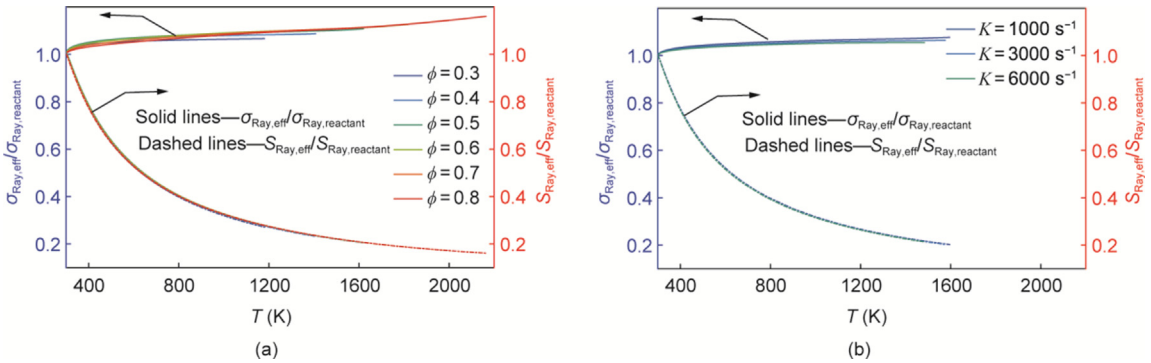

Fig. 5. Normalized Rayleigh scattering cross-section $\sigma_{Ray,eff}/\sigma_{Ray,reactant}$ and Rayleigh signal intensity $S_{Ray}/S_{Ray,reactant}$ over temperature T in lean premixed H_2/air flames (a) with varying equivalence ratios from 0.3 to 0.8 (lines largely overlap) and (b) with varying strain rates from 1000 to 6000 s^{-1} (lines largely overlap with each other) at constant equivalence ratio of 0.4.

and convolved with the filtered intensity image. Using this portion of the original image, the final determination of the flame front was based on the intensity gradient using the Canny algorithm as detailed in Ref. [27]. Along the flame front the local curvature was determined according to Ref. [57]. Intensity gradient and curvature were correlated to serve as TDI markers (Section 5.3).

5. Results and discussions

5.1. Laminar polyhedral flames

Fig. 6 shows time-averaged chemiluminescence images from the side Fig. 6(a) and from above Fig. 6(b), and horizontally aligned 2D OHPLIF images at a height of 5 mm above the burner Fig. 6(c). Due to the effective Lewis number of 0.58, positively curved troughs and negatively curved cusps were formed. Trough regions are characterized by elevated OH-PLIF intensities, whereas cusps regions show low signal intensities. For the operating conditions considered here, in the lower part of the flame 17 cells were observed with a mean cell size of 2.28 mm (at U_0 = 1.65 m·s^{-1}) and 2.52 mm (at U_0 = 2.50 m·s^{-1}), which is due to the different mean flame radius resulting from the different flow velocities and a constant laminar flame speed of 0.22 m·s^{-1} (Table 1). Similarly, the mean curvature of the troughs and cusps decreases with increasing flow velocity because of the enhanced velocity-induced strain and decreased residence time.

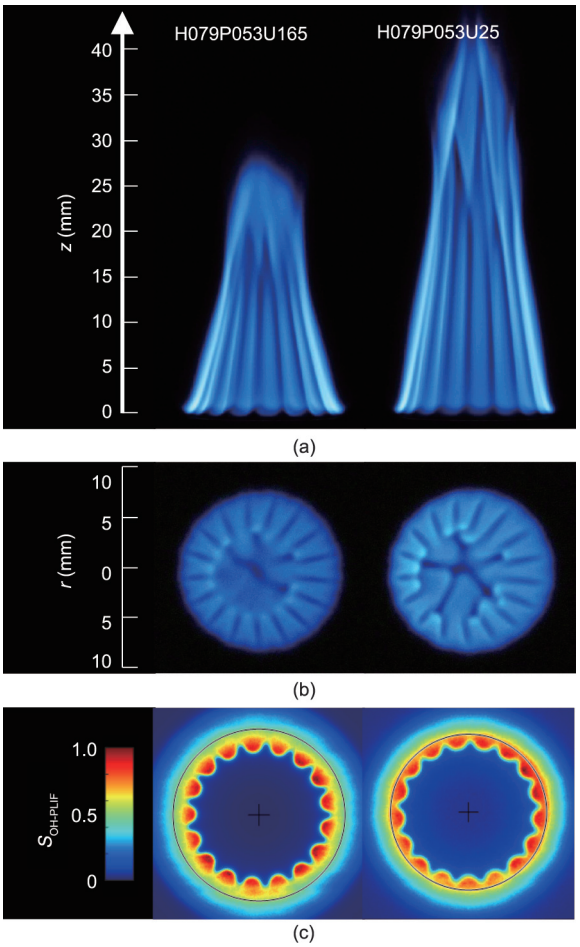

Fig. 6. (a) Side-view and (b) top-view flame images; and (c) OH-LIF image of laminar cases H079P053U165 (U_0 = 1.65 m·s^{-1}) and H079P053U250 (U_0 = 2.50 m·s^{-1}) [28].

In the positively (troughs) and negatively (cusps) curved flame zones, the increased preferential diffusion of H_2 and the effective Lewis number of 0.58 lead to a local change in the flame structure. To quantify these changes, 1D Raman/Rayleigh spectroscopy was used to measure scalar profiles perpendicular to the flame front in the center of both the trough and the cusp regions. Due to the 6 mm long measurement volume and the stationary flames, the molar fractions of the main species (H_2, O_2, CO, CO_2, H_2O, CH_4, and N_2), the temperature, and the equivalence ratio were quantified with a resolution of about 60 μm perpendicular to the flame front (Fig. 7). The zero point of the abscissa in the spatial profiles shown in Fig. 7 marks the point of the maximum CO mole fraction as a reference for comparing the two flames with the results of a 1D unstretched laminar flat flame simulation.

The measured scalar profiles in the cusp and trough region of the respective flames differ significantly from each other and from the 1D flame simulation. The strongest differences were found for the equivalence ratio and the hydrogen mole fraction. In the cusp region of flame H079P053U165 (U_0 = 1.65 m·s^{-1}), the mixture upstream of the flame front becomes leaner and reaches a minimum value of ϕ = 0.4, which is about 20 % below the global equivalence ratio of 0.53. Downstream of the flame front, the equivalence ratio slowly increases and reaches the global value 2.0 mm behind the flame front. This is different from the trough region where the minimum ahead of the flame front is only ϕ = 0.45 and aligns approximately with the steepest temperature gradient. Downstream the flame front, in the trough region, the increase in the equivalence ratio is more pronounced than in the cusp region, reaching a maximum of ϕ = 0.58 before decreasing towards ϕ = 0.53. Compared to the cusp regions, the gradients of the profiles in the troughs are steeper. This indicates faster transport, especially of H_2, and locally higher reaction rates.

When the bulk velocity is increased to 2.50 m·s^{-1}, the differences in the scalar profiles between the trough and cusp regions slightly decrease, in particular seen in the equivalence ratio profiles. This is consistent with the reduced curvature (Fig. 6), which weakens the focusing or defocusing of H_2 in positively or negatively curved regions. In agreement with Lulic et al. [58] and Weng et al. [59], the convergence of the scalar profiles for the cusp and trough regions with increasing bulk velocity is explained by the decreasing ratio of the convection timescale to the instability timescale, resulting from the inverse maximum of the growth rate.

5.2. Turbulent jet flames

The region of interest of the simultaneous OH-PLIF and PIV measurements was located between an axial position x/D = 6–8, centered around the 1D Raman/Rayleigh measurements at x/D = 7 (x = 31.5 mm). Following Peters [16], the turbulence–chemistry interaction was parameterized by the Karlovitz number Ka and the turbulent Reynolds number Re_T, calculated as using Eqs. (2) and (3). The turbulent rms velocity U' was obtained from the PIV measurements. Following Ref. [8], the integral length scales l was estimated by the half width at half maximum of the radial profiles of the mean axial velocities at an axial position of x/D = 7. For bulk velocities of 50 and 200 m·s^{-1}, the integral length scales decrease from 4.37 to 3.51 mm. As of the intense shear layer, U' increases with radius and peaks approximately at r/D = 0.75. This position coincides with the mean position of the flame front. The Karlovitz numbers Ka_C and Ka_F are calculated using U' from either the centerline position or its maximum position to estimate the range of Ka range numbers accessed by the jet flames at different bulk velocities. As bulk velocities increase from 50 to 200 m·s^{-1}, Ka_F increases from 50 to 730.

Although qualitative in nature, OH-PLIF was used to visualize instantaneous flame structures showing the effect of turbulence

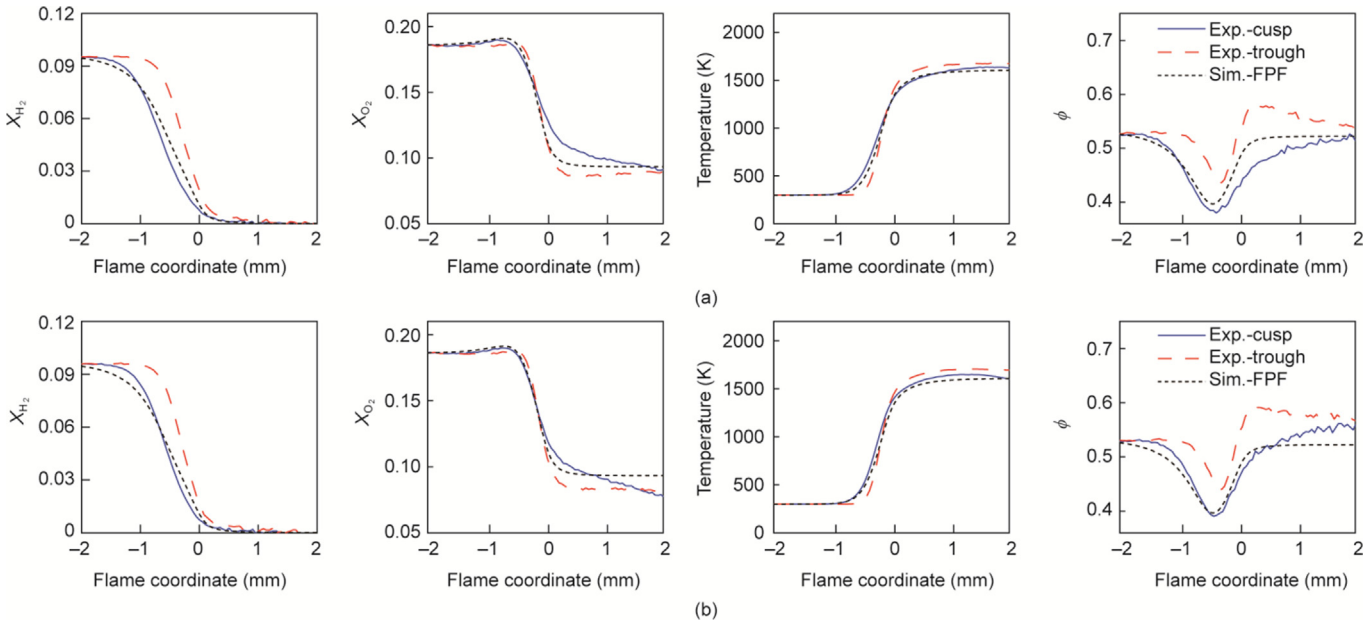

Fig. 7. Mole fractions, temperature, and equivalence ratio conditioned on the flame front for the laminar cases (a) H079P053U165 (U_0 = 1.65 m·s^{-1}) and (b) H079P053U250 (U_0 = 2.50 m·s^{-1}) [45].

interacting with TDIs in the trough and cusp regions. Fig. 8 shows individual snapshots of the flames with increasing bulk velocities. The maximum gradient of OH-PLIF intensities was used to detect the flame contour. An increasing OH gradient correlates with a higher local gas temperature. The flame contour was used to quantify the local flame surface mean curvature κ_m [60], color-coded in Fig. 8. For the lower bulk velocity case of U_0 = 50 m·s^{-1}, similar to

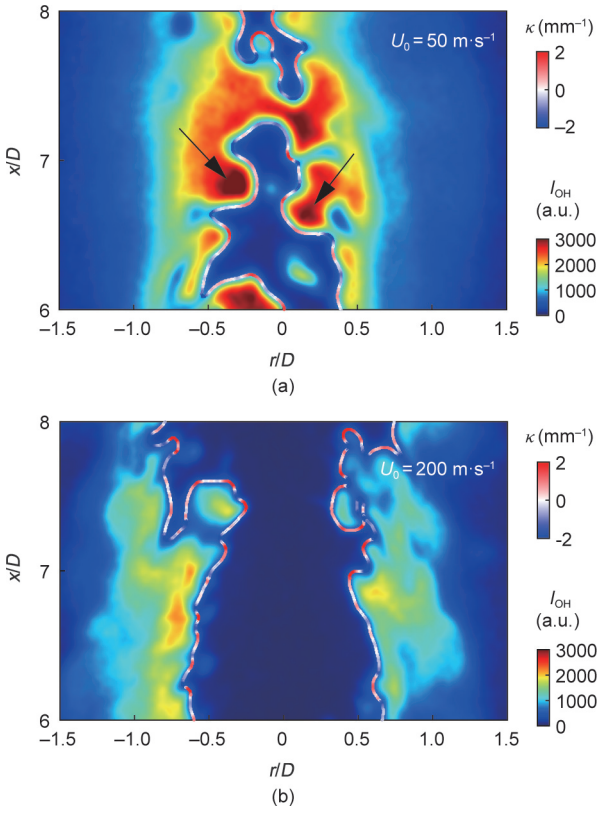

Fig. 8. Instantaneous flame images via OH-LIF of lean premixed hydrogen/air flame at bulk velocities of (a) 50 m·s^{-1} (case H100P040U050) and (b) 200 m·s^{-1} (case H100P040U200) [43].

the polyhedral flames, cellular flame structures with locally intense burning regions characterized by high OH signals are often observed (indicated by the arrows in Fig. 8). In particular, intensely burning regions with positive flame surface curvature (troughs) tend to have higher OH intensities because the highly diffusive H_2 is focused toward the burned side. Conversely, for flames with negative curvature (cusps), the highly diffusive H_2 is defocused.

Increasing the bulk velocity to U_0 = 200 m·s^{-1} results in more wrinkled flame surfaces associated with increasing curvature, while decreasing the size of cellular structures. This results in more homogeneous OH-PLIF signals along the reaction zone, indicating less spatial variation of the equivalence ratio, which is qualitatively similar to the polyhedral flame with higher bulk velocity (H079P053U250). In the highly turbulent case (U_0 = 200 m·s^{-1}) with Ka_F = 730, there is no evidence of local fuel enrichment due to preferential diffusion when inspecting the OH-PLIF images, although the flame surface is strongly curved. At these high velocities, the time scales for turbulent mixing are too short for H_2 to be focused (or defocused) by preferential diffusion across the curved flame surface. This is further analyzed in the following sections.

While OH-PLIF is used here for a qualitative visualization of the interplay between TDI and turbulence, 1D Raman/Rayleigh spectroscopy is used to quantify the influence of molecular diffusion and turbulent transport by measuring the local thermochemical state. Fig. 9 [43] shows the instantaneous internal flame structures for the two different bulk velocities. Fig. 9(a) shows the inverted 2D Rayleigh temperature fields with detected flame fronts using a temperature isoline and colored by the local mean curvature values. The temperature rise in the main reaction zone is clearly visible. The green dashed line marks the position of the 6 mm long 1D Raman/Rayleigh probe volume. The molar fractions measured by 1D Raman/Rayleigh spectroscopy for H_2 and H_2O are shown in Fig. 9(b). Values before (H_2) and after complete reaction (H_2O) for an unstretched planar flame are included as dashed green and blue lines, respectively. The temperature and equivalence ratios are shown in Fig. 9(c), where the dashed black and red lines mark the adiabatic flame temperature of 1427 K and the global equivalence ratio of ϕ_{global} = 0.4.

For a bulk velocity of 50 m·s^{-1}, superadiabatic temperatures are observed in the trough zones of high positive curvature. For the

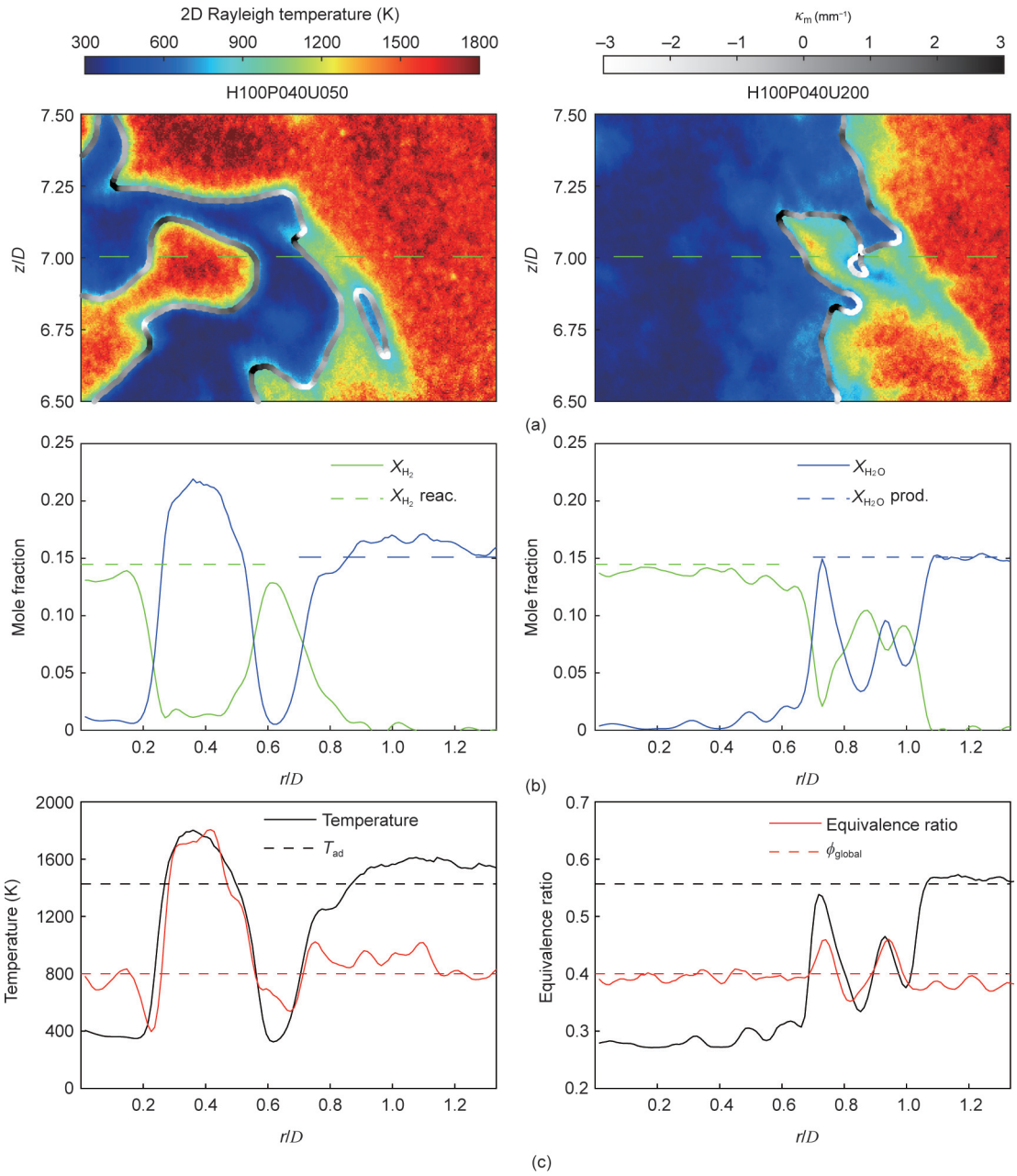

Fig. 9. Instantaneous (a) 2D Rayleigh temperature field with local flame front curvatures κ_m, (b) major reactant (reac.) and product (prod.) mole fractions, and (c) flame temperature and equivalence ratio of lean premixed hydrogen/air flames at bulk velocities of 50 m·s^{-1} (case H100P040U050) and 200 m·s^{-1} (case H100P040U200) [43].

snapshot shown, the flame front is strongly curved for radial positions r/D between 0.3 and 0.7. The local H_2 mole fraction in this region shows steep gradients, indicating thin reaction zones. The local equivalence ratio is strongly increased with values above 0.65 and is approximately 60% above the global value of 0.4, which supports findings from Refs. [61,62]. Correspondingly, superadiabatic temperatures with peaks of about 1800 K and local H_2O mole fractions of more than 0.2 are observed, which is significantly higher than the value of about 0.15 for a corresponding planar laminar flame. The trough regions with superadiabatic flame temperatures are due to effective Lewis numbers (Le_{eff}) below 1, since in these zones the heat is transported out slower than the H_2 is transported in. Comparing these local enhancements with those observed in the laminar polyhedral flames, synergistic interactions between TDI and turbulence are evident for this low Ka number flame.

As the bulk velocity is increased to 200 m·s^{-1}, the curvature of the flame fronts increases, as shown in the example image in Fig. 9(a) at the right hand side. On the one hand, the 1D scalar profiles show how the spatial distribution of the equivalence ratio becomes increasingly homogeneous (Fig. 9(c)). Accordingly, the probability of observing locally superadiabatic temperatures decreases. On the other hand, the reaction zone becomes increasingly distributed over larger volumes. This can be seen from the lower gradients (e.g. in the H_2 mole fraction), and non-monotonic scalar profiles are observed more frequently (Fig. 9(b)). This is since the turbulent time scales shorten with increasing Ka_F, while the molecular diffusion time scales decrease due to shallower gradients. At the fixed height of x/D = 7 above the burner considered here, the mean residence time is shortened with increasing bulk velocity to such an extent that there is no time for significant preferential diffusion of H_2 and thus for local fuel enrichment in the positively curved

flame sections. Therefore, at a Ka_F number of about 730, the profile of the equivalence ratio shown in Fig. 9(c) is approximately constant in space. This is clear experimental evidence that at highly turbulent H_2 flames, turbulent transport dominates over molecular transport.

The data presented so far is based on single events. The next step is to validate the observations statistically. For this purpose, 3000 individual laser shots are evaluated for each flame configuration at a measurement height of x/D = 7, which together comprise approximately 177 000 measurement points. Fig. 10 [43] shows the thermochemical states as a function of temperature using the conditional mean and standard deviation of the H_2 molar fraction (Fig. 10(a)), the H_2O molar fraction (Fig. 10(b)), and the equivalence ratio (Fig. 10 (c)). The adiabatic flame temperature is marked as a vertical dashed black line. Conditional means are shown as open squares, and the fluctuations (1σ) are shown as fluctuation bars. The results of the 1D laminar flame simulations for multicomponent transport and the assumption of a unity Lewis number are shown as solid blue and red lines, respectively. While the unity *Le* number simulations predict adiabatic temperatures, multicomponent simulations predict superadiabatic temperatures at maximum, which are lower than those observed in experiments due to the absence of curvature effects. These two cases can be considered as limiting cases for the thermochemical states of the system. The influence of preferential diffusion is clear from the profiles of the H_2 mole fraction and the equivalence ratio, while the correlation between the H_2O mole fraction and the temperature is only slightly affected. Superadiabatic temperatures are equally evident for all three scalars with states above the adiabatic temperature of 1427 K.

For the case with a bulk velocity of 50 m·s^{-1}, the H_2 mole fraction is in between the simulations. At low temperatures up to about 500 K, the decrease in the H_2 mole fraction is particularly pronounced, since H_2 diffuses toward the products ahead of the other species because of preferential diffusion in the preheating zone. This leads to a locally leaner mixture, which is particularly pronounced up to about 1100 K in the equivalence ratio profile with minimum conditional mean values of about 0.35, which qualitatively agrees with the observations in the polyhedral flames. For temperatures between 1100 K and the adiabatic flame temperature of 1427 K, the equivalence ratio initially increases only slightly and is close to 0.4 in the conditional mean. The small local minimum of the equivalence ratio observed near the adiabatic flame temperature is caused by measurements at the jet-pilot flow transition. For the superadiabatic temperature range above 1427 K, a rapid increase in the

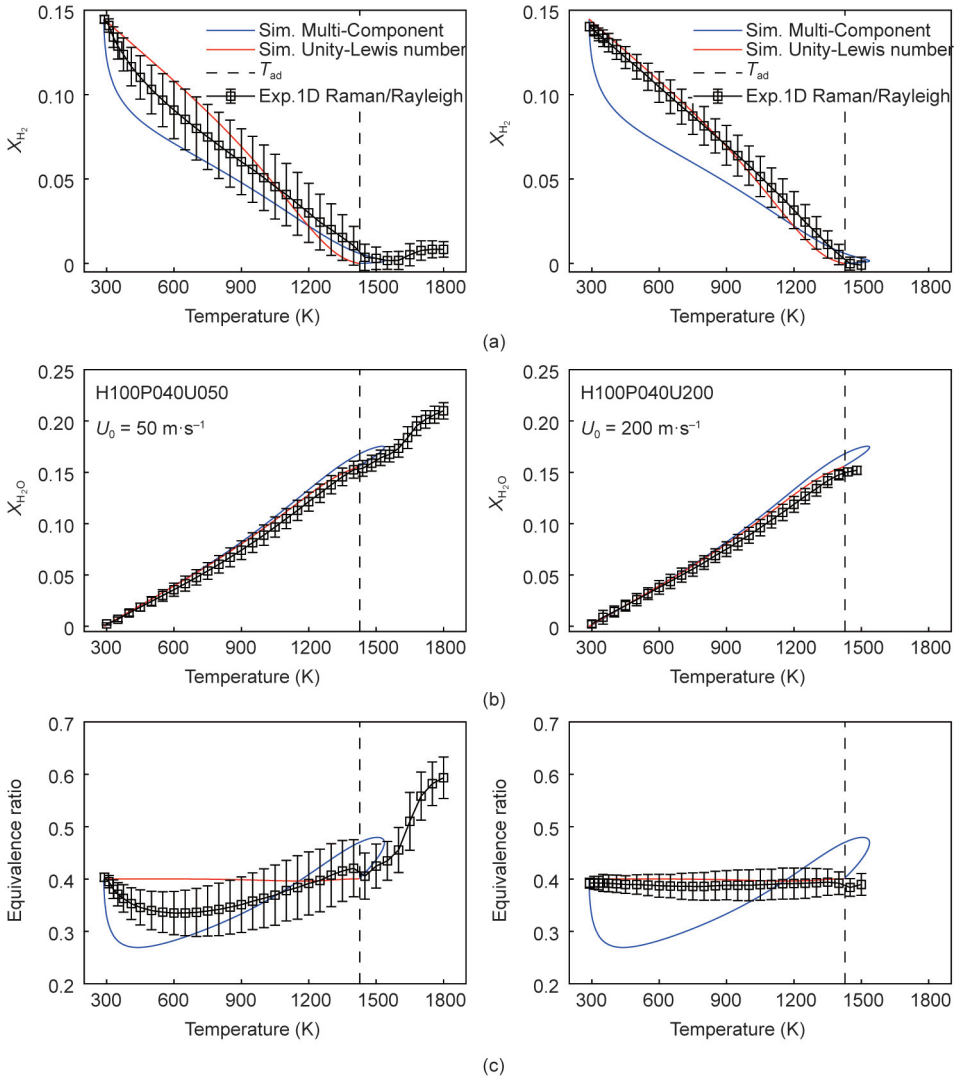

Fig. 10. Conditional mean distribution of (a) H_2 mole fraction, (b) H_2O mole fraction, and (c) equivalence ratio over temperature in lean premixed H_2/air turbulent flames for case 50 m·s^{-1} (case H100P040U050) and 200 m·s^{-1} (case H100P040U200) [43].

conditional mean values of the equivalence ratio up to about 0.6 is observed. The highest temperature of 1800 K is recorded in these flames. These superadiabatic conditions are statistically significant in this flame. In the range of superadiabatic temperatures, H_2O mole fractions with conditional averages up to about 0.21 are measured consistently with the elevated equivalence ratios. The deviation of the local equivalence ratio over wide temperature ranges and the high probability of the occurrence of superadiabatic temperatures are clear evidence for the preferential diffusion of H_2 and due to a low Lewis number. Both lead to an accumulation of H_2 and heat in regions of high positive flame curvature. These experimental results confirm previous DNS predictions [1], which, however, assumed homogeneous isotropic turbulence conditions and thus differ significantly from the shear flow turbulence used here.

As the bulk velocity and thus the Ka_F number are increased, the conditional mean values of all three scalars approach the unity Lewis number simulation. Superadiabatic flame temperatures become rarer, but do not disappear completely, and peak around 1500 K. Here, the H_2O mole fraction corresponds to the equilibrium value of a global equivalence ratio of 0.4, and the H_2 mole fraction is consistently close to zero with small statistical fluctuations. In agreement with the individual events shown in Fig. 9, this behavior now also shows statistically that with increasing turbulence the influence of TDIs decreases and almost disappears at Ka_F numbers above 700. For the correlation between equivalence ratio and temperature, this results in a flattening, or, in other words, the equivalence ratio remains almost constant over the reaction zone. Furthermore, the turbulent fluctuations decrease significantly with increasing *Ka* number, although the flame curvatures become more intense.

This behavior, in turn, confirms predictions from DNS [1] that the influence of molecular transport processes disappears above a critical *Ka* number. In the DNS, as in the experiment, a globally lean H_2/air mixture with an equivalence ratio of 0.4 was used. The critical *Ka* number where molecular transport processes have no noticeable influence on the thermochemical state lies in the experiment at about 730, which is significantly lower than the critical *Ka* number of over 1500 predicted by the DNS [1]. There are several reasons for this. On the one hand, the DNS assumes homogeneous isotropic turbulence, whereas in the experiment the flame is stabilized in a turbulent shear layer. On the other hand, there is a pilot flame in the experiment, which leads to different thermal boundary conditions, especially near the outer part of the shear layer, than in the DNS, where a flame propagating through a fresh gas mixture at 300 K is analyzed.

5.3. Internal combustion engine

The combination of flame front imaging and quantitative scalar diagnostics based on Raman and Rayleigh scattering cannot be used in the ICE. Therefore, other measures are required to determine the effect of TDIs in the turbulent flame. In Ref. [27], it was proposed to correlate the intensity gradient of qualitative OH-PLIF images in the reaction zone with the corresponding curvature. A strong positive curvature and a steep intensity gradient indicate the trough region of a TDI, while the simultaneous occurrence of negative curvature with low intensity gradients indicates a cusp region. This concept has been transferred to SO_2-PLIF in the hydrogen-fueled ICE. Fig. 11 [46] shows that steep intensity gradients in the SO_2-PLIF image correlate with zones of high positive curvature, and low intensity gradients correlate with negative curvatures. Thus, the magnitude *R*, as the Pearson correlation coefficient between intensity gradients and curvature, is used as a TDI marker in the engine to assess the extent to which cellular structures have formed.

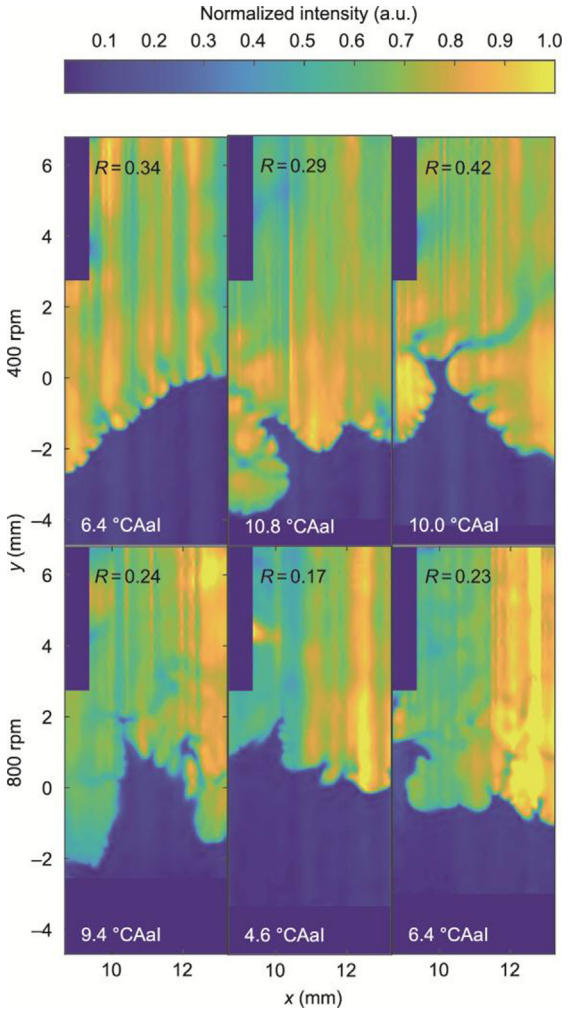

Fig. 11. SO_2-PLIF intensity distribution of individual realizations after denoising, dewarping, intensity correction, and normalization for 400 rpm (top) and 800 rpm (bottom) at three selected times during early flame spread. The three individual images are taken from a sequence acquired at a resolution of 0.4 CA (400 rpm, case H100P040R400) and 0.6 CA (800 rpm, case H100P040R800), respectively [46].

Fig. 11 [46] shows individual images of the denoised, normalized, and intensity-corrected SO_2-PLIF signals for three instants at the early stage of flame kernel growth, together with the values of the corresponding TDI markers (*R*-values at the top of each image). The images are from different engine cycles at different timings after spark ignition (degree crank angle after ignition (°-CAaI)), indicated by the crank angles values at the bottom of each image. Remaining vertical stripes are due to fluctuations in laser excitation and beam steering that cannot be compensated by normalization to the mean spatial laser energy distribution. Although the flame fronts show finger-like structures typical of TDIs at both 400 and 800 rpm, these structures are more pronounced at the lower engine speed, which is also reflected in the *R*-values, which are higher by up to a factor of two.

For statistical analysis, 400 cycles for both engine speeds are considered to support the observations from the individual images. Fig. 12 [46] shows histograms, probability density functions (PDF), and cumulative distribution functions (CDF) for both engine speeds. Although the distributions overlap, it is evident that the values for the TDI marker are higher at lower speeds. This is reflected in the mean values of the distributions, which are significantly higher at 400 rpm (μ_{400} = 0.24) than at 800 rpm (μ_{800} = 0.16).

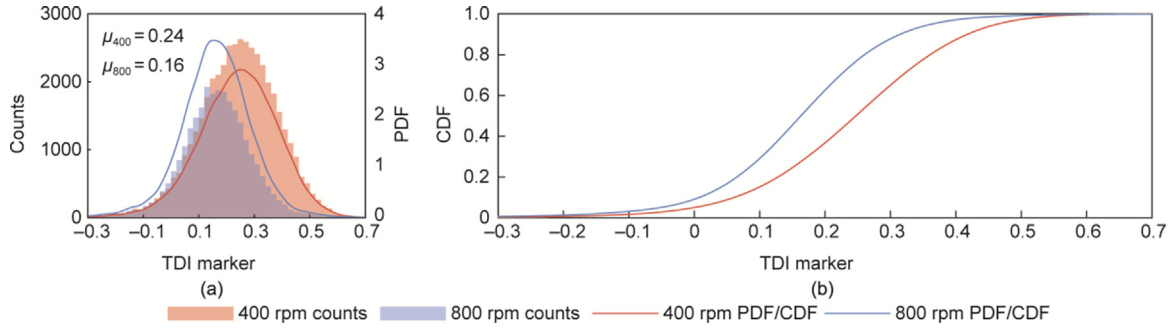

Fig. 12. (a) Distribution of *R*-values for 400 and 800 rpm shown as histogram and PDF with the mean values for the respective conditions μ. (b) Corresponding CDF for 400 and 800 rpm [46].

In general, the more pronounced TDI at low engine speeds might be attributed to differences in gas temperature, pressure, and turbulence intensity, but at first it is unclear which effect dominates. From the measured pressure curves, assuming isentropic conditions (γ = 1.4) and using the gas properties from Cantera calculations [63], the gas temperatures for the two speeds were estimated. For the ignition time (0° CAaI), the temperature at 800 rpm was found to be about 45 K higher compared to 400 rpm. This difference decreased to 11 K at 16° CAaI. However, based on DNS studies [40,41], significantly higher temperature differences of about 200 K are required to cause a 35% change in cell size. Inspection of Fig. 11 shows that the change in cell structure size is higher when switching from 800 to 400 rpm, so the higher gas temperature at the higher speed cannot be the main cause for the differences in the distribution of the *R*-values. To investigate the influence of pressure, the *R*-value distributions for cylinder pressures of (12 ± 0.25) bar were compared for the two engine speeds. It was found that the two distributions retained the differences. Thus, the slightly different evolution of the pressure curves due to the different ignition times is likewise not a primary cause for the different levels of TDI. As discussed in Ref. [64], for the tumble plane of this ICE, the turbulence intensity increases significantly with engine speed under otherwise identical boundary conditions. This implies that the increase in turbulence intensity with speed is the primary driver for mitigating TDI at 800 rpm, supporting recent results of simulation studies [65].

Even though the formation of TDI cells is significantly reduced at higher engine speeds, the increase in flame speed caused by TDIs must be considered. This must be reflected in the numerical simulations used for engine design. Current research is therefore investigating how TDI influences turbulent flame wrinkling and thus flame speed, and how this can be modeled. TDI causes higher local NO_x formation due to superadiabatic temperatures. The effects of TDI on wall heat transfer and flame extinction remain open questions in H_2 engine research. Consequently, further investigation of TDI in combustion engines is essential to accurately model and further develop H_2-powered engines.

6. Conclusions

The use of hydrogen as a renewable energy carrier in technical combustion processes requires a better understanding of the specific combustion properties resulting from its high diffusion rate and high chemical reactivity. The formation of TDI in lean premixed hydrogen/air flames is one consequence of these special properties. These instabilities can cause significant local variations in the flame structures, resulting not only in an increase in the local combustion speed, but also in the formation of zones with superadiabatic temperatures, potentially leading to higher thermal nitrogen oxide formation. In technical combustion systems, TDI are superimposed by turbulence, which in turn lead to the deformation of flame fronts. Although it is generally known that the effects of TDI decrease with increasing turbulence, depending on the ratio of the time scales between molecular diffusion and turbulent transport, a quantitative measurement of these effects for hydrogen/air flames has only recently been performed. These recent advancements are summarized in this review.

This review focuses on ① how the effects of TDI on the thermochemical states in the reaction zone can be measured quantitatively using *in situ* laser spectroscopy; ② how increasing levels of turbulence intensities and turbulence properties affect TDI; and ③ how the interaction between turbulence and TDI can be quantified at high pressures where the access for optical diagnostics is very limited. Experimental studies were conducted using three configurations: laminar lean premixed H_2/CH_4/air polyhedral flames; piloted turbulent lean premixed H_2/air jet flames; and propagating flames in the early combustion phase after ignition in a lean premixed H_2-fueled ICE. The measurements are based on Raman/Rayleigh scattering and laser-induced fluorescence. The combination of these methods allows flame topologies such as local curvatures and scalar gradients to be measured simultaneously with temperatures and major species concentrations from which the local equivalence ratio is determined. While these methods are very useful in open configurations, their application in confined combustion systems under pressure, such as internal combustion engines, is limited. For this reason, this review also presents how topological properties can be used to infer the formation of TDI.

In lean laminar H_2/CH_4/air polyhedral flames, the internal structure of the reaction zone is strongly influenced by preferential diffusion and the imbalance between hydrogen diffusion and heat conduction (*Le*-number effect). This leads to the formation of intrinsic instabilities that manifest themselves as curved flame fronts with cusp and trough regions of slightly different magnitudes of curvature. The negatively and positively curved flame fronts result in different scalar profiles. The differences are particularly pronounced in the H_2 mole fraction and the equivalence ratio, as well as in the gradients of these quantities. Although this phenomenon has been known for a long time, this study is the first to experimentally quantify the effects of TDI on the internal flame structure, which is defined by local thermochemical states including species concentration and temperatures.

The investigations under turbulent flow conditions show, in agreement with polyhedral flames, that the effects of TDI decrease with increasing flow velocity. At low Karlovitz numbers, strongly developed trough zones are found in the turbulent jet flame, where the local equivalence ratio is greatly increased, leading to superadiabatic temperatures. Here, the scalar gradients are very steep, which favors the rapid diffusion of H_2 into the positively curved flame zones. At high Karlovitz numbers, the flames are more

curved because of the more intense turbulence, but the focusing of hydrogen associated with locally increased equivalence ratios and superadiabatic flame temperatures occurs much less frequently. Under extreme turbulence, TDI are suppressed approaching the distributed burning regime. This trend is similar under high pressure conditions in the propagating flame of an ICE. Here, the degree of turbulence is varied by varying the engine speed rather than by increasing the bulk velocity. While the TDI are clearly visible at 400 rpm, they are less pronounced at 800 rpm. To quantify this trend, the intensity gradient of the SO_2 fluorescence is correlated with the local flame curvature. Statistical analysis of hundreds of engine cycles shows quantitatively how turbulence dominates molecular transport processes when increasing the engine speed.

The experimental investigations were aimed at the quantitative determination of the interaction between TDI and flows with different properties. In addition, the data are available upon request for validation of mathematical models in numerical simulations.

CRediT authorship contribution statement

Tao Li: Writing – original draft, Visualization, Project administration, Methodology, Investigation, Funding acquisition, Formal analysis, Conceptualization. **Benjamin Böhm:** Writing – review & editing, Supervision, Project administration, Methodology, Funding acquisition. **Andreas Dreizler:** Writing – original draft, Supervision, Resources, Project administration, Funding acquisition, Conceptualization.

Declaration of competing interest

The authors declare that they have no known competing financial interests or personal relationships that could have appeared to influence the work reported in this paper.

Acknowledgments

The authors acknowledge the support by the European Research Council (ERC; 101119058–HYROPE–ERC-2023-SyG) and the German Research Foundation (DFG; 556960810 and FOR 2687–423224402).

References

[1] Aspden AJ, Day MS, Bell JB. Turbulence–flame interactions in lean premixed hydrogen: transition to the distributed burning regime. J Fluid Mech 2011;680:287–320.
[2] Aspden AJ, Day MS, Bell JB. Lewis number effects in distributed flames. Proc Combust Inst 2011;33(1):1473–80.
[3] Lipatnikov AN, Chomiak J. Molecular transport effects on turbulent flame propagation and structure. Pror Energy Combust Sci 2005;31(1):1–73.
[4] Steinberg AM, Hamlington PE, Zhao X. Structure and dynamics of highly turbulent premixed combustion. Pror Energy Combust Sci 2021;85:100900.
[5] Driscoll JF. Turbulent premixed combustion: flamelet structure and its effect on turbulent burning velocities. Pror Energy Combust Sci 2008;34(1):91–134.
[6] Driscoll JF, Chen JH, Skiba AW, Carter CD, Hawkes ER, Wang H. Premixed flames subjected to extreme turbulence: some questions and recent answers. Pror Energy Combust Sci 2020;76:100802.
[7] Law C, Sung C. Structure, aerodynamics, and geometry of premixed flamelets. Pror Energy Combust Sci 2000;26(4–6):459–505.
[8] Zhou B, Brackmann C, Li Q, Wang Z, Petersson P, Li Z, et al. Distributed reactions in highly turbulent premixed methane/air flames. Combust Flame 2015;162(7):2937–53.
[9] Zhou B, Brackmann C, Li Z, Aldén M, Bai XS. Simultaneous multi-species and temperature visualization of premixed flames in the distributed reaction zone regime. Proc Combust Inst 2015;35(2):1409–16.
[10] Zhou B, Brackmann C, Wang Z, Li Z, Richter M, Aldén M, et al. Thin reaction zone and distributed reaction zone regimes in turbulent premixed methane/air flames: scalar distributions and correlations. Combust Flame 2017;175:220–36.
[11] Fan Q, Liu X, Xu L, Subash AA, Brackmann C, Aldén M, et al. Flame structure and burning velocity of ammonia/air turbulent premixed flames at high Karlovitz number conditions. Combust Flame 2022;238:111943.
[12] Cai X, Fan Q, Bai XS, Wang J, Zhang M, Huang Z, et al. Turbulent burning velocity and its related statistics of ammonia–hydrogen–air jet flames at high Karlovitz number: effect of differential diffusion. Proc Combust Inst 2023;39(4):4215–26.
[13] Dunn MJ, Masri AR, Bilger RW. A new piloted premixed jet burner to study strong finite-rate chemistry effects. Combust Flame 2007;151(1–2):46–60.
[14] Dunn MJ, Masri AR, Bilger RW, Barlow RS, Wang GH. The compositional structure of highly turbulent piloted premixed flames issuing into a hot coflow. Proc Combust Inst 2009;32(2):1779–86.
[15] Dunn MJ, Masri AR, Bilger RW, Barlow RS. Finite rate chemistry effects in highly sheared turbulent premixed flames. Flow Turbul Combus 2010;85(3–4):621–48.
[16] Peters N. Turbulent combustion. Cambridge: Cambridge University Press; 2000.
[17] Wabel TM, Skiba AW, Driscoll JF. Turbulent burning velocity measurements: extended to extreme levels of turbulence. Proc Combust Inst 2017;36(2):1801–8.
[18] Wabel TM, Skiba AW, Temme JE, Driscoll JF. Measurements to determine the regimes of premixed flames in extreme turbulence. Proc Combus Inst 2017;36(2):1809–16.
[19] Temme J, Wabel TM, Skiba AW, Driscoll JF. Measurements of premixed turbulent combustion regimes of high Reynolds number flames. In: Proceedings of 53rd AIAA Aerospace Sciences Meeting, American Institute of Aeronautics and Astronautics; 2015 Jan 5–9; Kissimmee, Florida. AIAA; 2015.
[20] Wabel TM, Skiba AW, Driscoll JF. Evolution of turbulence through a broadened preheat zone in a premixed piloted Bunsen flame from conditionally-averaged velocity measurements. Combust Flame 2018;188:13–27.
[21] Skiba AW, Wabel TW, Carter CD, Hammack SD, Temme JE, Driscoll JF. Premixed flames subjected to extreme levels of turbulence part I: flame structure and a new measured regime diagram. Combus Flame 2018;189:407–32.
[22] Li X, Wang Z, Li T, Dreizler A, Lipatnikov AN, Liu X, et al. Investigation of burning velocity of lean and rich premixed NH_3/H_2 turbulent flames using multi-scalar imaging. Proc Combust Inst 2024;40(1–4):105541.
[23] Wang Z, Li X, Li T, Dreizler A, Mousavi SM, Lipatnikov AN, et al. Experimental investigation of NH_3–H_2 jet flames adopting multiscalar imaging: comparison of turbulent burning velocities obtained using different flame-front markers. Combust Flame 2025;275:114054.
[24] Wang Z, Li X, Li T, Dreizler A, Lipatnikov AN, Liu X, et al. Experimental investigation of internal structures of $NH_3/H_2/O_2/N_2$ premixed jet flames using multi-scalar imaging. Proc Combust Inst 2024;40(1–4):105436.
[25] Schultheis R, Li T, Shi S, Barlow RS, Zhou B, Geyer D, et al. Quantitative measurements of thermo-chemical states in turbulent lean and rich premixed $NH_3/H_2/N_2$–air jet flames. Proc Combust Inst 2024;40(1–4):105571.
[26] Li T, Shi S, Schultheis R, Wang Z, Geyer D, Zhou B, et al. Flame and flow characteristics of lean premixed turbulent $NH_3/H_2/N_2$–air flames with increasing Karlovitz numbers. J Ammonia Energy 2025;3(1).
[27] Chaib O, Hochgreb S, Boxx I. An experimental marker of thermo-diffusive instability in hydrogen-enriched flames. Proc Combust Inst 2024;40(1–4):105763.
[28] Shi S, Breicher A, Trabold J, Hartl S, Barlow RS, Dreizler A, et al. Cellular structures of laminar lean premixed H_2/CH_4/air polyhedral flames. Appl Energy Combus Sci 2023;13:100105.
[29] Zhang W, Wang J, Lin W, Mao R, Xia H, Zhang M, et al. Effect of differential diffusion on turbulent lean premixed hydrogen enriched flames through structure analysis. Int J Hydrogen Energy 2020;45(18):10920–31.
[30] Hochgreb S. How fast can we burn, 2.0. Proc Combust Inst 2023;39(2):2077–105.
[31] Salazar V, Kaiser S. Influence of the flow field on flame propagation in a hydrogen-fueled internal combustion engine. SAE Int J Engines 2021;4(2):2376–94.
[32] Aleiferis PG, Rosati MF. Flame chemiluminescence and OH LIF imaging in a hydrogen-fuelled spark-ignition engine. Int J Hydrogen Energy 2012;37(2):1797–812.
[33] Leite CR, Brequigny P, Borée J, Foucher F. Early flame development characterization of ultra-lean hydrogen–air flames in an optical spark-ignition engine. Proc Combust Inst 2024;40(1–4):105260.
[34] Welch C, Erhard J, Shi H, Dreizler A, Böhm B. An experimental investigation of lean hydrogen flame instabilities in spark-ignition engines. Proc Combust Inst 2024;40(1–4):105391.
[35] Berger L, Attili A, Pitsch H. Synergistic interactions of thermodiffusive instabilities and turbulence in lean hydrogen flames. Combus Flame 2022;244:112254.
[36] Pitsch H. The transition to sustainable combustion: hydrogen- and carbon-based future fuels and methods for dealing with their challenges. Proc Combus Inst 2024;40(1–4):105638.
[37] Lipatnikov AN, Chomiak J. Effects of premixed flames on turbulence and turbulent scalar transport. Pror Energy Combust Sci 2010;36(1):1–102.
[38] Aspden AJ, Day MS, Bell JB. Turbulence–chemistry interaction in lean premixed hydrogen combustion. Proc Combust Inst 2015;35(2):1321–9.
[39] Aspden AJ, Day MS, Bell JB. Towards the distributed burning regime in turbulent premixed flames. J Fluid Mech 2019;871:1–21.
[40] Berger L, Attili A, Pitsch H. Intrinsic instabilities in premixed hydrogen flames: parametric variation of pressure, equivalence ratio, and temperature. Part 1—dispersion relations in the linear regime. Combust Flame 2022;240:111935.

[41] Berger L, Attili A, Pitsch H. Intrinsic instabilities in premixed hydrogen flames: parametric variation of pressure, equivalence ratio, and temperature. Part 2—non-linear regime and flame speed enhancement. Combust Flame 2022;240:111936.
[42] Howarth TL, Hunt EF, Aspden AJ. Thermodiffusively-unstable lean premixed hydrogen flames: phenomenology, empirical modelling, and thermal leading points. Combust Flame 2023;253:112811.
[43] Shi S, Schultheis R, Barlow RS, Geyer D, Dreizler A, Li T. Internal flame structures of thermo-diffusive lean premixed H_2/air flames with increasing turbulence. Proc Combust Inst 2024;40(1–4):105225.
[44] Shi S, Schultheis R, Barlow RS, Geyer D, Dreizler A, Li T. Assessing turbulence–flame interaction of thermo-diffusive lean premixed H_2/air flames towards distributed burning regime. Combust Flame 2024;269:113699.
[45] Shi S, Breicher A, Schultheis R, Hartl S, Barlow RS, Geyer D, et al. Structures of laminar lean premixed H_2/CH_4/air polyhedral flames: effects of flow velocity, H_2 content and equivalence ratio. Flow Turbul Combus 2024;113(4):1081–110.
[46] Ye P, Erhard J, Shi H, Dreizler A, Böhm B. Analysis of thermodiffusive instabilities and flame front wrinkling in a hydrogen-fueled engine. Proc Combust Inst 2025;41:105884.
[47] Bouvet N, Halter F, Chauveau C, Yoon Y. On the effective Lewis number formulations for lean hydrogen/hydrocarbon/air mixtures. Int J Hydrogen Energy 2013;38(14):5949–60.
[48] Mei B, Zhang J, Shi X, Xi Z, Li Y. Enhancement of ammonia combustion with partial fuel cracking strategy: laminar flame propagation and kinetic modeling investigation of NH_3/H_2/N_2/air mixtures up to 10 atm. Combust Flame 2021;231:111472.
[49] Baum E, Peterson B, Surmann C, Michaelis D, Böhm B, Dreizler A. Investigation of the 3D flow field in an IC engine using tomographic PIV. Proc Combust Inst 2013;34(2):2903–10.
[50] Baum E, Peterson B, Böhm B, Dreizler A. On the validation of LES applied to internal combustion engine flows: part 1: comprehensive experimental database. Flow Turbul Combus 2014;92(1–2):269–97.
[51] Trabold J, Butz D, Schneider S, Dieter K, Barlow R, Dreizler A, et al. Fast shutter line-imaging system for dual-dispersion Raman spectroscopy in ethanol and OME flames. Combus Flame 2022;243:111864.
[52] Fuest F, Barlow RS, Geyer D, Seffrin F, Dreizler A. A hybrid method for data evaluation in 1D Raman spectroscopy. Proc Combus Inst 2011;33(1):815–22.
[53] Barlow RS, Dunn MJ, Sweeney MS, Hochgreb S. Effects of preferential transport in turbulent bluff-body-stabilized lean premixed CH_4/air flames. Combus Flame 2012;159(8):2563–75.
[54] Honza R, Ding CP, Dreizler A, Böhm B. Flame imaging using planar laser induced fluorescence of sulfur dioxide. Appl Phys B 2017;123(9):246.
[55] Renaud A, Ding CP, Jakirlic S, Dreizler A, Böhm B. Experimental characterization of the velocity boundary layer in a motored IC engine. Int J Heat Fluid Flow 2018;71:366–77.
[56] Otsu N. A threshold selection method from gray-level histograms. IEEE Trans Syst Man Cybern 1979;9(1):62–6.
[57] Wen X, Zirwes T, Scholtissek A, Böttler A, Zhang F, Bockhorn H, et al. Flame structure analysis and composition space modeling of thermodiffusively unstable premixed hydrogen flames—part I: atmospheric pressure. Combus Flame 2022;238:111815.
[58] Lulic H, Breicher A, Scholtissek A, Lapenna PE, Dreizler A, Creta F, et al. On polyhedral structures of lean methane/hydrogen Bunsen flames: combined experimental and numerical analysis. Proc Combus Inst 2023;39(2):1977–86.
[59] Weng Y, Potnis A, Saha A. Regime and morphology of polyhedral Bunsen flames. Combus Flame 2023;248:112585.
[60] Li T, Zhou B, Frank JH, Dreizler A, Böhm B. High-speed volumetric imaging of formaldehyde in a lifted turbulent jet flame using an acousto-optic deflector. Exp Fluids 2020;61(4):112.
[61] Chen YC, Bilger RW. Experimental investigation of three-dimensional flame-front structure in premixed turbulent combustion. Combus Flame 2004;138(1–2):155–74.
[62] Wu MS, Kwon S, Driscoll JF, Faeth GM. Preferential diffusion effects on the surface structure of turbulent premixed hydrogen/air flames. Combust Sci Technol 1991;78(1–3):69–96.
[63] Goodwin DG, Moffat HK, Schoegl I, Speth RL, Weber BW. Cantera: an object-oriented software toolkit for chemical kinetics, thermodynamics, and transport processes. Software. Pasadena: California Institute of Technology; 2023.
[64] Zentgraf F, Baum E, Böhm B, Dreizler A, Peterson B. On the turbulent flow in piston engines: coupling of statistical theory quantities and instantaneous turbulence. Phys Fluids 2016;28(4):045108.
[65] Chu H, Berger L, Grenga T, Wu Z, Pitsch H. Effects of differential diffusion on hydrogen flame kernel development under engine conditions. Proc Combust Inst 2023;39(2):2129–38.